Synthetic Aperture Radar Radiometric Cross Calibration Based on Distributed Targets

Yongsheng Zhou , *Member, IEEE*, Li Zhuang, Jitong Duan , Fan Zhang , *Senior Member, IEEE*, and Wen Hong, *Senior Member, IEEE*

Abstract—Synthetic aperture radar (SAR) radiometric calibration is an essential step in inferring meaningful physical information about the target. The majority of current calibration processes are directly based on artificial calibrators, but the number of calibrators is always restricted. Cross calibration, which has been widely used for optical and meteorological satellites, performs calibration by another calibrated satellite. Distributed targets are used as the calibration reference, allowing for frequent calibration. However, the potential of introducing cross calibration to SAR satellites has not been confirmed, and two issues must be resolved: 1) the number of calibration targets available for cross calibration is limited to a few known distributed targets; 2) the imaging parameters of calibrated and uncalibrated SARs are different, which may cause errors when cross calibration is applied. In this article, a method for selecting stable distributed targets using time-series stability analysis was presented first. The saline–alkali land and urban areas were selected as the calibration targets with low and high backscattering, respectively. Second, different stable pixel extraction methods were adopted based on the characteristics of different targets. Third, the Oh model was used to correct the scattering difference caused by the incidence angle difference, which greatly improved the accuracy of the backscattering coefficients of the calibration targets. The cross calibration experiments on the same series of satellite (Sentinel-1 A/B) data revealed that the accuracy of cross calibration was comparable to the accuracy of the artificial calibrator-based method, with a difference of less than 0.48 dB (1σ).

Index Terms—Cross calibration, radiometric calibration, synthetic aperture radar (SAR), scattering stability, stable target.

I. INTRODUCTION

SYNTHETIC aperture radar (SAR) radiometric calibration [1] is an essential step in inferring meaningful information about the physical parameters of a target, which forms

a prerequisite for qualitative and quantitative remote sensing applications [2], [3], [4]. The normalized radar cross section (NRCS) of distributed targets and the radar cross section (RCS) of a corner reflector are two examples of physically meaningful quantities that are converted from image digital numbers (DN) during the radiometric calibration process. [5], [6], [7].

The rapid development of spaceborne SAR technology has created an urgent need for operational high-frequency radiometric calibration [8], [9], [10], [11], [12], [13], [14]. The majority of currently used external radiometric calibration methods rely on the deployment of artificial calibrators as reference targets at the calibration site, as shown in Fig. 1(a). The artificial calibrators must be evenly distributed over tens of kilometers of the SAR image scene. Thus, it is usually very labor-intensive and time-consuming to deploy artificial calibrators in the field. In addition, the operating parameters of active calibrators are usually designed for a single SAR sensor. They are difficult to share with other SAR sensors that operate at drastically different incidence angles or operating frequencies. With the launch of more SAR satellites and constellation satellites, the implementation of this approach becomes unfeasible due to the difficulties in increasing the number of artificial calibrators, thus emphasizing the need for alternative SAR calibration methods [15].

The cross calibration method, which has been widely utilized in optical imaging and meteorological satellites [16], [17], [18], [19], has the ability to address the drawbacks of conventional SAR radiometric calibration, as shown in Fig. 1(b). The already calibrated SAR satellite data are used to perform radiometric calibration of the SAR data to be calibrated. In other words, the backscattering coefficients of the SAR satellite images to be calibrated can be obtained from the backscattering coefficients of the calibrated SAR satellite images. This approach can avoid the deployment of many artificial calibrators and is not constrained by the satellite revisit time.

However, due to the differences in imaging mechanisms between SAR and optical/meteorological sensors, cross calibration cannot be directly applied to SAR calibration, and there are two issues that need to be addressed as follows.

1) The number of reference targets available for cross calibration is limited to a few known distributed targets, such as the Amazon rainforest [20], [21]. From the basic process of SAR calibration, to increase the calibration frequency, the imaging frequency of the calibration targets must be significantly increased. However, the revisit time of the spaceborne SAR sensor is fixed when the orbit
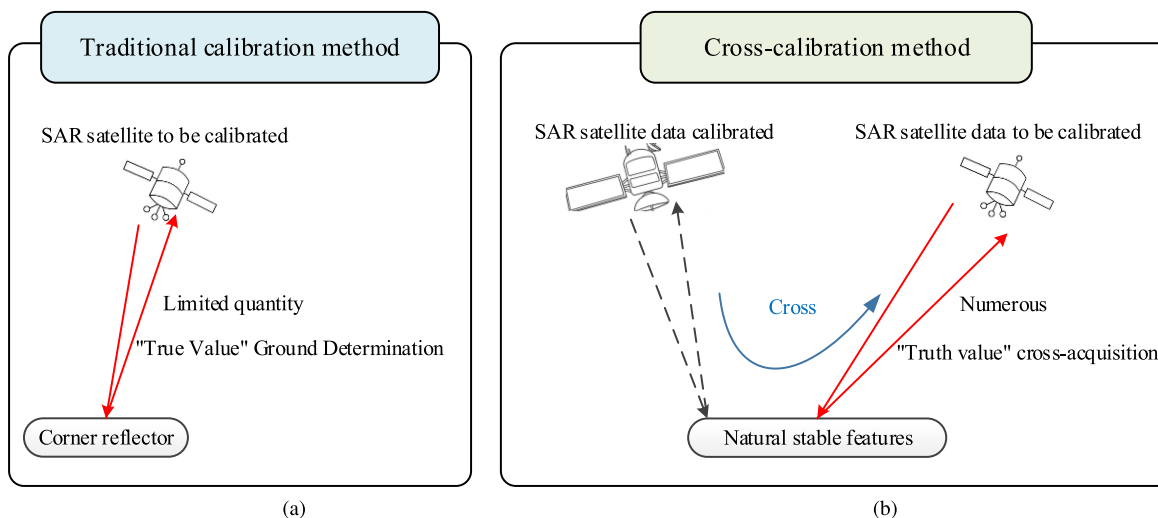
Fig. 1.   Comparison of calibration methods.

is determined. Therefore, it is necessary to increase the number of calibration targets significantly. The Amazon rainforest was proposed for the estimation of the SAR antenna pattern in the 1980 s and is still in use today. D'Aria et al. [22] proposed a radiometric stability monitoring method combining natural permanent scatterers (PS) with artificial calibrators. This PS-based calibration method is characterized by its intrinsic robustness due to the consensus of many natural targets. Yang et al. [23] demonstrate that the median center value of the backscattering coefficients in urban areas is a statistically stable feature. After filtering the urban dataset through the neural network, the final calibration accuracy is within 0.5 dB. These studies illustrate the feasibility of using natural stable targets for radiometric calibration. However, these studies are only for one kind of calibration target, and the number of stable calibration targets needs to be expanded. The rational selection of the targets that exist in nature can effectively increase the number of calibration targets. Stable targets in nature include point-like targets (e.g., parabolic satellite antennas) and uniformly distributed targets (e.g., rainforests, deserts, saline–alkali land). These targets are widely present in nature in large numbers. In this article, a method for selecting stable calibration targets is presented. The calibration targets are selected on the basis of the stability of the time series scattering. Depending on the characteristics of different targets, different stable pixel extraction methods are applied. By these methods, the number of stable pixels can be effectively increased for cross calibration.

2) The imaging parameters (e.g., incidence angle) of calibrated and uncalibrated SARs are different [24], which may result in calibration errors if cross calibration is applied directly. The radiometric calibration process is based on the correlation between the image digital number and the backscattering coefficient. So it is crucial to accurately obtain the backscattering coefficients of the

data to be calibrated. Some scholars have studied other calibration targets that can replace the Amazon rainforest for site-free calibration, such as oil spill platforms, oceans, and deserts [25], [26], [27], [28]. However, when analyzing the scattering characteristics of these ground objects, it is found that the scattering characteristics of these ground objects depend on imaging parameters like incidence angle, polarization, and operation frequency. Calibration errors will occur if the backscattering coefficients from calibrated SAR imaging conditions are utilized as the backscattering coefficients from uncalibrated SAR imaging conditions. There are many scattering models, such as the Oh model [29], Dubois model [30], and the advanced integrated equation model (AIEM) [31] that can be used for surface parameter inversion [29], [32], [33]. Based on the calibrated SAR data, we can use the inversion models (such as the Oh model, Dubois model, and AIEM model) to obtain the surface parameters. Assuming the surface parameters remain unchanged, we can use the corres ponding forward models to obtain the backscattering coefficients under the uncalibrated SAR imaging parameters. In this article, based on the selected stable distribution targets, we propose a method based on the Oh model [29], [34] to correct the scattering difference caused by the incidence angle difference between calibrated SAR and uncalibrated SAR, which can effectively improve the accuracy of the cross calibration.

In general, the main contributions of this article are as follows.
1) To address the problem of insufficient stable calibration targets, stability analysis of the scattering characteristics of various ground objects is carried out, and the saline–alkali and urban areas are selected as stable reference distributed targets. The median value is selected to extract the backscattering coefficients of the nonuniform calibration targets, which effectively reduces the errors caused by extreme points or registration of nonuniform calibration targets.

2) Regarding the difference in incidence angle between calibrated and uncalibrated SARs, the Oh scattering model is introduced into the cross calibration process. The difference in incidence angle is corrected by the Oh model, which effectively improves the calibration accuracy.

The rest of this article is organized as follows. Section II briefly reviews some related work. Section III presents detailed methods for stable target selection, pixel extraction, and incidence angle correction. Section IV presents the experimental results on the Sentinel-1 A/B dataset. Finally, Section V concludes this article.

II. BASIC PRINCIPLES AND RELATIVE WORK

A. Basic Principles of SAR Calibration

The purpose of SAR radiometric calibration is to obtain the scattering characteristics (radar cross section or backscattering coefficient) of the target. Through the relationship between the pixel power of the target and the backscattering coefficient, the total transfer function of the SAR system can be obtained. The formula is as follows:

$$\sigma = \frac{1}{H} P_r \tag{1}$$

where P_r is the target pixel power, H is the total transfer function, and σ is the backscattering coefficient. SAR radiation calibration is the process of accurately calculating the total transfer function H, but there are many sources of error throughout the SAR data acquisition chain. The radiometric calibration formula that accounts for changes in various system parameters and imaging geometry is as follows:

$$\sigma^0 = \frac{DN_{i,j}^2}{K} \frac{R^3}{R_{\text{ref}}^3} \frac{\sin \theta_{i,j}}{\sin \theta_{\text{ref}}} \frac{1}{G(\theta)^2} \tag{2}$$

where DN represents the pixel value in the ith row and jth column, K is the absolute calibration coefficient, which is a constant. θ is the incidence angle of the distance to each pixel in the SAR image. θ_{ref} is the incidence angle of the reference point, such as artificial corner reflectors and active calibrators. R is the slant distance value of each pixel point in the range direction. R_{ref} is the slant distance value of the reference point. $G(\theta)^2$ is the gain value of the antenna. It is a function of the incidence angle in the distance direction.

Artificial corner reflectors and active calibrators are traditionally used as calibration reference targets. However, the availability of these artificial targets is often restricted, which limits the calibration frequency. In recent years, natural targets, which are abundant in nature, have been gradually used as calibration reference targets.

B. Radiometric Calibration Based on Natural Point Targets

Point targets in nature are Earth surface targets with strong radar scattering responses that are comparable to the responses of artificial calibrators in SAR images, both of which have a high signal cluster ratio. They are initially studied in the permanent scatterer interferometric synthetic aperture radar (PS-InSAR)

technique and then introduced to the SAR radiometric calibration. In 1999, Usai et al. [35] found that exposed rocks and artificial buildings (e.g., roads and houses) in SAR images showed high coherence over a long time scale. Their coherence was studied over the entire time series and could reverse surface deformation. On this basis, Ferretti et al. [36] proposed the PS-InSAR technique. The basic idea is to filter the points on the time-series SAR images that are less affected by decoherence, extract and solve the differential phase model of these points, and extract the deformation phase. In 2010, D'Aria et al. [22] proposed an SAR radiometric calibration method based on an artificial calibrator and permanent scatterers. The permanent scatters enable continuous radiometric calibration and avoid the time-consuming and laborious problems of using solely artificial calibrators. In 2014, Guccione et al. [37] extracted point targets from natural permanent scatterers and applied them to SAR long-term relative radiometric calibration and antenna pointing tests. It achieved an accuracy of 1 dB. In 2018, Guccione et al. [38] also used stable point targets for L/P band SAR radiometric calibration and antenna pattern estimation. In 2019, Du et al. [39] verified the feasibility of using parabolic antennas for spaceborne P-band polarimetric SAR calibration.

Although radiometric calibration based on natural point targets can solve the problem of insufficient artificial calibrators, Biancardi et al. [40] point out two limitations of such methods. First, the image scene must contain point targets, such as buildings and rocks, requiring approximate imaging conditions, which are difficult to apply for cross calibration between different SAR satellites. Second, to extract permanent scatterers, long-time interferometric SAR data are needed, and the interferometric processing is very complex. In addition, the side lobes of point targets can also lead to radiometric errors and require additional corrections [15], [41], [42].

C. Radiometric Calibration Based on Natural Distributed Targets

Distributed targets in nature are large areas of the earth's surface with similar scattering. Typical distributed targets include farmland, grassland, bare land, etc. In 1985, Moore et al. proposed using the Amazon rainforest to estimate the antenna pattern of spaceborne SAR [43]. Its primary purpose was to determine the direction of the SIR-B two-way pitch antenna from the SIR-B digital image of the Amazon rainforest. The Amazon rainforest was used not only because it is the world's largest, flattest, most stable distributed target, but also because its backscattering coefficient hardly varies with the incidence angle due to the volume scattering properties of the rainforest. However, the number of tropical rainforests used for calibration is limited; for example, the Amazon rainforest and several rainforests in Canada. It is difficult to increase the frequency of SAR imaging with calibration targets. Other distributed uniform targets in nature (e.g., crops, bare land, and deserts) are suitable for calibration under specific conditions [44]. In 2018, Yang et al. [23] analyzed C-band SAR images and found that the median center of gravity of the backscattering coefficients in urban areas had good temporal stability. Its accuracy reaches

0.21 dB, which is equivalent to the nominal absolute radiometric accuracy. Zakharov et al. [45] proposed monitoring the radiometric stability of the ALOS/PALSAR and PALSAR-2 satellites using the Caspian Sea oil platform. The results show that the SAR sensor has a backscattering stability of 0.6 dB per year. The stability of distributed uniform targets, such as Chile's Atacama Desert, the Amazon rainforest, and the permanent ice sheet in Antarctica, is also found to be comparable to that of artificial corner reflectors. The stability of the radiometric calibration of Lake Vostok in Antarctica even reaches 0.19 dB in 3.5 years.

Although these studies show that radiometric calibration using distributed uniform targets is possible, the conclusions above were reached using the same SAR imaging parameters. The backscattering coefficients of most natural targets tend to vary with imaging parameters like the incidence angle. Therefore, the natural targets are difficult to directly apply for cross calibration, and their backscattering coefficients must be corrected according to different imaging parameters. For point targets, it is difficult to estimate and correct for this variation, but distributed targets can be estimated and corrected based on the target's backscattering model. In this article, we begin by selecting distributed uniform targets with stable backscattering coefficients. The stability of the backscattering coefficient is incorporated into the calibration requirements for the calibration targets to construct an SAR calibration target database that meets the needs of radiometric cross calibration.

D. SAR Cross Calibration

Cross calibration of remote sensing sensors refers to using the data from calibrated sensors to calibrate the data to be calibrated. Cross calibrations of optical imaging satellites and meteorological satellites have been extensively studied [16], [17], [18], [19], while there are few studies similar to or related to SAR cross calibration in the past decades.

Zink et al. [46] reported a cross-calibration flight experiment with airborne E-SAR/DC-8 SAR sensors in 1989. Forty-two trihedral corner reflectors, four dihedral corner reflectors, an active calibrator, and a receiver were deployed as calibration targets. The experimental results showed that cross calibration was feasible when the reflector pointing was precisely adjusted, the antenna pattern was known, and the flight trajectory and platform attitude data were known. The backscattering coefficients of the distributed targets are relatively consistent, with differences of less than 2 dB. The authors noted that this difference was due to differences in incidence angle and soil moisture. In 2014, Zakharov et al. [47] used a parabolic antenna as a calibration target to cross-compare the radiometric stability of the ERS AMI scatterometer and the ENVISAT ASAR. The radiometric stability of the former is 1 dB higher than the latter's. It is worth mentioning that this work uses an artificial calibrator precisely pointed at the SAR sensor. In practice, it is challenging to implement cross calibration for natural calibration targets whose orientation cannot be controlled and whose directional scattering characteristics are unknown.
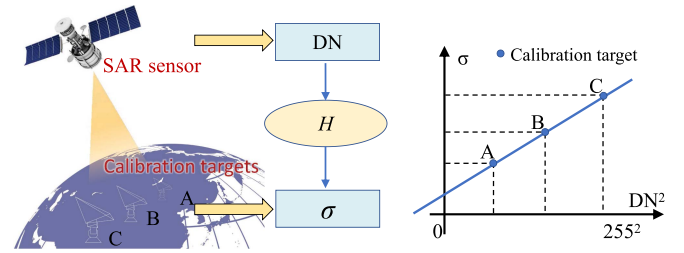

Fig. 2. Traditional SAR calibration process.

III. METHODOLOGY

Fig. 3 shows the overall flow chart of the proposed SAR cross radiometric calibration method based on distributed targets. It mainly consists of four parts, namely, the selection of stable targets, the extraction of stable pixels, the correction of SAR imaging parameter differences, and the calculation of the calibration coefficient.

A. Selection of Stable Distributed Targets

Cross calibration is based on imaging the same target scene with calibrated and uncalibrated SAR. In this approach, it is assumed that the target scene maintains the same physical characteristics. In other words, the calibration targets for cross calibration need to meet the stability requirements for the backscattering coefficients.

The backscattering coefficient is related to soil moisture, surface roughness, dielectric constant, incidence angle, etc. It can be expressed as

$$\sigma = f(\theta, \lambda, P, s, m_v, \epsilon, \dots) \tag{3}$$

where θ is the incidence angle related to the SAR imaging geometry, λ is wavelength, and P represents the polarization related to the SAR system parameters. m_v, s, and ϵ represent soil moisture, surface root mean square height, and dielectric constant, respectively. They are associated with the physical characteristics of the target. Cross calibration requires that the physical characteristics of the selected calibration targets remain relatively stable. In other words, the soil moisture (m_v), surface root mean square height (s), and dielectric constant (ϵ) should remain stable during the cross calibration. They are essential for selecting stable targets and improving the cross calibration accuracy.

The stability of the physical characteristics corresponds to the time-series stability of the backscattering coefficients of the calibration target when the incidence angle (θ) and the polarization of the sensor (P) remain constant (same satellite and same incidence angle). The backscattering coefficient is determined by two factors, i.e., the satellite system and the observed ground objects. If the system's parameters, such as its operating frequency, the incidence angle, and other parameters, are the same, the only factor affecting the changes in backscattering coefficient will be the characteristics of the ground objects [such as soil moisture (m_v), surface root mean square height (s), and dielectric constant (ϵ)]. In this instance, the higher the stability of
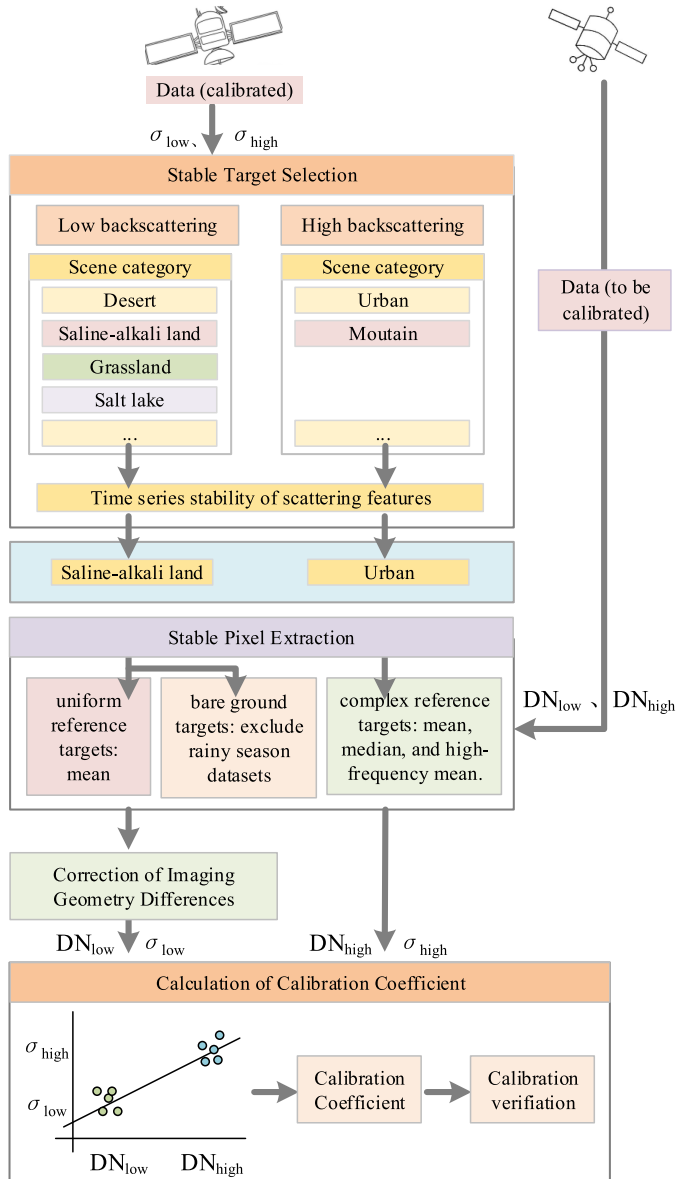
Fig. 3. Overall flow chart of the proposed SAR cross radiometric calibration method based on distributed targets.

the backscattering coefficient, the more stable the characteristics of the ground objects.

In this article, the selection of stable distributed targets is carried out by investigating the time-series stability of the backscattering coefficients of different candidate distributed target scene categories. First, two sets of SAR data from the same satellite are obtained, with different imaging times but the same flight direction and incidence angle. Then the standard deviation STD of the backscattering coefficients between the two sets of data is calculated, since the standard deviation measures the dispersion of the mean of a set of data. The smaller the standard deviation, the more stable the backscattering coefficients are. A threshold is set in order to select the target. The target scene category should not be utilized as cross calibration reference targets if

Algorithm 1: Selection of Stable Distributed Targets.

Input: Two dataset acquired in different dates: D_x and D_y; the block size of the distributed target $m * n$;
Output: $Result$;
Data preprocessing (include orbit correction, radiometric calibration, range-Doppler terrain correction) by SNAP;
Data registration;
Extract the distributed target blocks and their backscattering
coefficients σ_x and σ_y;
$\sigma_u = \text{mean}(\sigma_y)$;
$\text{sum} = 0$;
for i in $(0,1,...,m * n)$ **do**
 $\text{sum} = \text{sum} + (\sigma_x(i) - \sigma_u)^2$;
end for
$\text{STD} = \sqrt{\frac{1}{m*n}\text{sum}}$;
if $\text{STD} \leq 1 \ dB$ **then**
 $Result = 1$;
else
 $Result = 0$;
end if

the standard deviation is higher than the threshold, but they can be utilized as reference targets if the standard deviation is lower than the threshold. The threshold set in this experiment is 1 dB.

The detailed process of selecting a stable distributed target is shown in Algorithm 1.

B. Stable Pixel Extraction

Not all pixels within the selected distributed calibration target are used for cross calibration. Stable pixels are extracted in the following two cases: 1) If the selected stable target is a uniform area with a single type of ground feature, the mean value within a block is directly taken as the stable DN/backscattering coefficient. 2) If the environment is complicated and there are many extreme points in the selected stable target, the extreme points need to be removed. For example, some scholars use urban areas as a source to obtain stable high backscattering coefficients [48]. However, urban areas have a complex environment with the coexistence of roads, trees, bridges, and houses. To remove the extreme points, this article adopts three methods for DN/backscattering coefficient extraction: 1) the median method, 2) the mean method, and 3) the high-frequency mean method. The high-frequency mean is calculated as follows: Divide the minimum value to the maximum value of the backscattering coefficients into ten intervals, calculate the frequency of the backscattering coefficients in each interval, and calculate the average value of the backscattering coefficients in the interval, where the frequency is greater than 10%. The data extraction by the method can also achieve a certain level of noise filtering to avoid errors caused by noise.

In cross calibration, to ensure the stability of the backscattering coefficient, it is necessary to ensure that the physical parameters, including soil moisture (m_v), do not vary much.

Algorithm 2: Stable Pixel Extraction.

> **Input:** The backscattering coefficient of the dataset σ_0;
> the digital number of dateset DN; type of reference
> target T_0; the reference target is bare ground T_{bare};
> **Output:** σ_0, DN;
> **if** $T_0 = T_{\text{uniform}}$ **then**
> $\sigma_0 = \text{mean}(\sigma_0)$;
>   DN = mean(DN);
> **else** [$//T_0 = T_{\text{complex}}$]
> $\sigma_0 = \min(\text{mean}(\sigma_0), \text{median}(\sigma_0),$
>   high frequency average(σ_0));
>   DN = min(mean(DN), median(DN),
>   high frequency average(DN));
> **end if**
> **if** T_{bare} **then**
> $\sigma_0 = \sigma_0(\text{exclude rainy season})$;
>   DN = DN(exclude rainy season);
> **end if**

Fig. 4.   Method for obtaining backscattering coefficient of data to be calibrated.

Since soil moisture (m_v) is more susceptible during the rainy season compared to other physical parameters, the stability of the selected target is ensured by analyzing the time-series stability of the backscattering coefficient. In this article, if the target is not bare ground (such as urban), the effect of the rainy season on the backscattering coefficient is not analyzed. If the target is bare (such as saline–alkali land), we can examine whether the rainy season affects the backscattering coefficient by adding the time series variation of the backscattering coefficient with and without the rainy season data. If the backscattering coefficient varies significantly between the rainy season and other seasons, the data from the rainy season data can be removed from the data of this calibration target. Whether the rainy season data need to be deleted depends on the acquisition time of the two datasets. If one dataset is in the rainy season and the other is not, calibration should not be performed. This operation avoids the effect of changes in soil moisture on the backscattering coefficient.

The detailed process of extracting stable pixels is shown in Algorithm 2.

C. Correction of Imaging Parameter Differences

SAR cross calibration is using the calibrated data to calibrate the uncalibrated data. It is necessary to consider the variation of the backscattering coefficients of the calibration targets caused by differences in the incidence angle, radar wavelength, polarization, terrain slope, etc. The problem is mathematically described as

$$\begin{cases} \sigma_1 = f(\theta_1, \lambda_1, P_1, s_1, m_{v1}, \epsilon_1, \ldots) \\ \sigma_2 = f(\theta_2, \lambda_2, P_2, s_2, m_{v2}, \epsilon_2, \ldots) \end{cases} \quad (4)$$

where f denotes the backscattering model of the calibration target; σ_1 and σ_2 are the backscattering coefficients of the target when illuminated by the calibrated SAR and the SAR to be calibrated, respectively.

When stable reference targets and pixels are selected and extracted using the methods in Section III-A and III-B, it can be
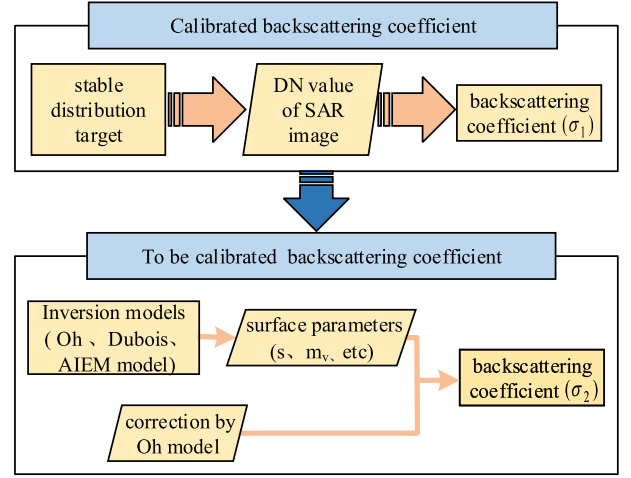
considered that $s_1 = s_2, m_{v1} = m_{v2}, \epsilon_1 = \epsilon_2$. Then, we can use the calibrated SAR data to obtain the surface parameters by the inversion models, assuming that the surface parameters remain unchanged, and then obtain the backscattering coefficients under the uncalibrated SAR imaging parameters by the corresponding forward models

$$\begin{aligned} \arg\min_{s,m,\epsilon} & \left(|f(s, m, \epsilon;\ \theta_1,\ \lambda_1,\ P_1,\ \ldots) - \sigma_1| \right) \\ \rightarrow\ & \sigma_2 = f(s, m, \epsilon;\ \theta_2,\ \lambda_2,\ P_2,\ \ldots). \end{aligned} \quad (5)$$

The process for obtaining the backscattering coefficient σ_2 is shown in Fig. 4.

The Oh model [29] is used as the surface scattering model f in this article. It is an empirical model accounting for the SAR data of bare ground with different surface roughness, soil moisture, wave bands, incidence angles, and polarizations

$$\sigma_{vh}^0 = 0.11 m_v (\cos\theta)^{2.2} [1 - \exp(-0.32(ks)^{1.8}] \quad (6)$$

$$p = \frac{\sigma_{hh}^0}{\sigma_{vv}^0} = 1 - \left(\frac{2\theta}{\pi}\right)^{0.32 m_v^{0.65}} \exp(-0.4(ks)^{1.4}) \quad (7)$$

$$\begin{aligned} q &= \frac{\sigma_{vh}^0}{\sigma_{vv}^0} \\ &= 0.095(0.13 + \sin 1.5\theta)^{1.4}(1 - \exp(-1.3(ks)^{0.9})) \quad (8) \end{aligned}$$

where m_v represents soil moisture, θ represents incidence angle, k represents wave number, s represents surface root mean square height, p represents copolarization ratio, and q represents cross-polarization ratio. The Oh model is chosen because it can be applied to SAR data with a wide range of surface roughness, X-, C-, and L-bands, and an incidence angle between 10 and 70.

If all parameters except the incidence angle are the same or approximate, the Oh model can be used to derive the backscattering coefficients to be calibrated at different incidence angles. According to (6), the relationship between the calibrated SAR data and the SAR data to be calibrated in VH polarization can

be expressed as

$$\frac{\sigma_{vh1}}{\sigma_{vh2}} = \frac{\cos(\theta_1)^{2.2}}{\cos(\theta_2)^{2.2}}. \tag{9}$$

On the other hand, according to (8), the calibrated SAR data and the SAR data to be calibrated can be expressed as

$$\sigma_{vh1} = 0.095(0.13 + \sin 1.5\theta_1)^{1.4}(1 - \exp(-1.3(ks)^{0.9}))\sigma_{vv1}^0 \tag{10}$$

$$\sigma_{vh2} = 0.095(0.13 + \sin 1.5\theta_1)^{1.4}(1 - \exp(-1.3(ks)^{0.9}))\sigma_{vv2}^0. \tag{11}$$

By dividing (10) with (11) and combining (9), we can obtain

$$\frac{\sigma_{vh1}}{\sigma_{vh2}} = \frac{(0.13 + \sin 1.5\theta_1)^{1.4}\sigma_{vv1}}{(0.13 + \sin 1.5\theta_2)^{1.4}\sigma_{vv2}} = \frac{\cos(\theta_1)^{2.2}}{\cos(\theta_2)^{2.2}}. \tag{12}$$

Rewriting (12), the relationship between the calibrated SAR data and the SAR data to be calibrated in VV polarization can be expressed as

$$\sigma_{vv1} = \frac{\cos(\theta_1)^{2.2}(0.13 + \sin 1.5\theta_2)^{1.4}}{\cos(\theta_2)^{2.2}(0.13 + \sin 1.5\theta_1)^{1.4}}\sigma_{vv2}. \tag{13}$$

The derived backscattering coefficients in (9) and (13) can then be used to calibrate the SAR satellite data to be calibrated.

D. Calculation of Calibration Coefficient

In this article, calibration targets with stable high and low backscattering coefficients are used for radiometric calibration. The model corrects the backscattering coefficient of the calibrated SAR satellite to obtain the backscattering coefficient of the SAR satellite to be calibrated. Two points are used to determine a straight line. The high and low backscattering coefficients are combined to fit the calibration coefficients in the radiometric calibration process. The calibration equation is as follows:

$$\sigma = m \cdot \text{DN}^2 + n \tag{14}$$

where σ is the backscattering coefficient of the SAR satellite data to be calibrated obtained by this method. The DN value is the digital quantization value of the corresponding pixel in the SAR satellite data to be calibrated. m is the calibration coefficient of the SAR satellite data to be calibrated. n is the calibration offset value of the SAR satellite data to be calibrated.

IV. EXPERIMENT AND DISCUSSION

To quantitatively analyze the accuracy and effectiveness of the proposed SAR cross calibration method based on distributed targets, the Sentinel-1 (S-1) SAR dataset is used. The time series stability of different reference targets, the stability of the urban target under different extraction methods, the error of the backscattering coefficient caused by the incidence angle, and the stability of the backscattering coefficient of urban and saline–alkali land in the 12-month SAR data are presented. Finally, based on the above research, in the Dunhuang area, Sentinel-1B data are calibrated based on Sentinel-1 A data.
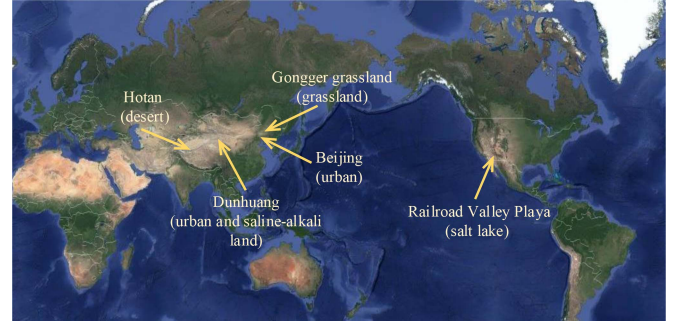

Fig. 5. Location of the study area.

A. Study Area and Experiment Dataset

The study area of this article includes the urban area of Beijing, China; the saline–alkali land and urban area of Dunhuang, China; the salt lake area of Railroad Valley Playa, USA; the desert area of Hotan, China; and the grassland area of Gongger, China. The locations of the datasets are shown in Fig. 5. The selection of these study areas is according to the well-known optical calibration sites. The CEOS Working Group on Calibration and Validation (WGCV) provides calibration sites with good uniformity, rich types, and clear latitude and longitude data. They are good candidate sites for SAR cross-calibration. But not all optical calibration sites can be used for SAR cross calibration. We need to select from the optical calibration sites.

The Sentinel-1 SAR data are then obtained for these study areas. Sentinel-1 (S-1) is the European flagship SAR mission, initiated by the European Space Agency and the European Commission. It is a constellation of two C-band twin satellites that provide backscattering on a global scale [49]. The Sentinel-1 C-band-based imaging system uses four imaging modes, including stripes (SM), wide interference (IW), ultra-wide (EW), and wave mode (WV). Sentinel-1 has a very high radiometric accuracy of 1 dB. This article uses Sentinel-1 data in dual polarization IW imaging mode.

These data are used to analyze the scattering stability and extract the backscattering coefficients. The initial data need to be preprocessed. Data preprocessing includes orbit correction, radiometric correction, and terrain correction. The state information of the orbit is refined, and the distance distortion is improved. It establishes the relationship between the digital values of the images and the values of the backscattering coefficients. Data preprocessing is performed using the sentinel application platform (SNAP). The sentinel application platform is the basic platform of all Sentinel toolboxes and is a desktop CS platform. It has extensibility, portability, and modular interface.

B. Stable Low Backscattering Target Selection and Pixel Extraction

The process of selecting stable targets with low backscattering coefficients is performed among candidate distributed targets of grassland, salt lake, desert, and saline–alkali land. All four calibration targets have backscattering coefficients below -10 dBm^2/m^2. Their time series stability is analyzed using data

TABLE I
SPECIFIC INFORMATION OF THE SENTINEL-1 A DATASET

Scene category	Time	Location	Data size
Saline-alkali land	2018/06/22	Dunhuang	90×90
Saline-alkali land	2018/03/18	Dunhuang	110×110
Desert	2018/06/15	Hotan	90×90
Desert	2018/03/11	Hotan	110×110
Salt lake	2018/06/22	Railroad Valley Playa	90×90
Salt lake	2018/03/18	Railroad Valley Playa	110×110
Grassland	2018/06/24	Gongger Grassland	90×90
Grassland	2018/03/20	Gongger Grassland	110×110
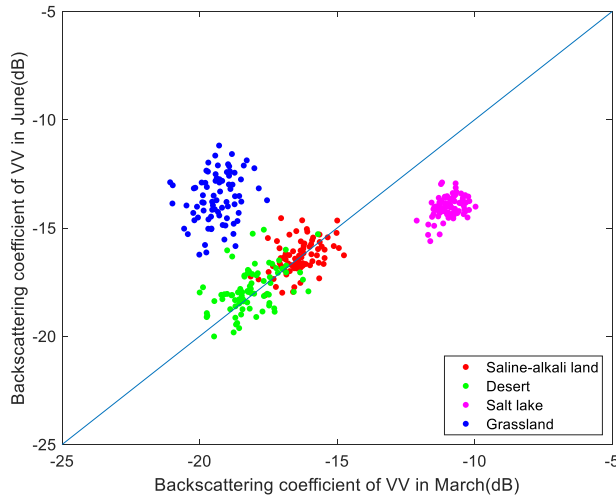
Fig. 6. Variations of backscattering coefficients of four distributed targets between March and June.

Fig. 7. Time series stability analysis of saline–alkali land.

from Sentinel-1 A. Sentinel-1 A calibrated data in March and June of the same year are used to analyze the variation of the backscattering coefficient. The SAR imaging time difference is three months (June and March) because it spans a season.

The specific information of the Sentinel-1 A dataset is shown in Table I. For more precise registration, the data sizes are initially cropped differently. After the registration is completed, all data sizes become 90×90 pixels.

Fig. 6 shows the variation of the backscattering coefficients for the different calibration targets between March and June. It is clear that the desert and saline–alkali land are stable because their data distributions are consistent with the $y = x$ line.

Table II shows a comparison of the standard deviation of the backscattering coefficients between March and June. The smaller the standard deviation, the more minor the variation of the backscattering coefficients with time, and the more stable the scattering characteristics of the calibration target.

According to Fig. 6 and Table II, the saline–alkali land has the most stable backscattering coefficients, and its standard deviations the VV and VH polarization are lower than those of other targets. The saline–alkali land is a type of salt accumulation, which affects crop growth normally. According to incomplete statistics from the United Nations Educational, Scientific and Cultural Organization (UNESCO) and the Food and Agriculture Organization of the United Nations (FAO), the area of
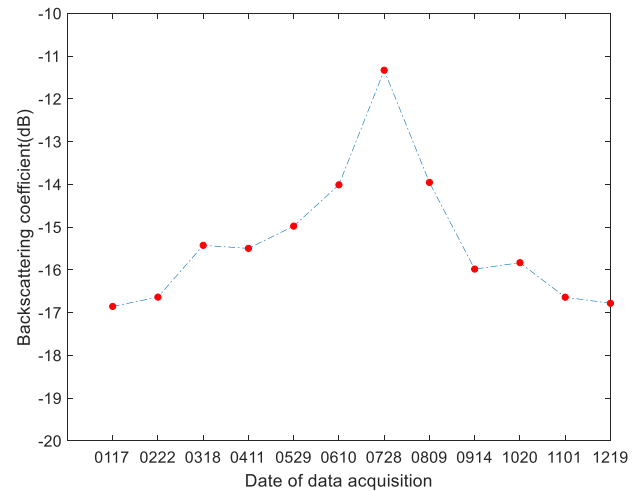
saline–alkali land in the world is 954.38 million hectares, widely dispersed across more than 30 countries on six continents. It is mainly distributed in India, Pakistan, Russia, South Africa, and other countries. It can be noticed from Table II that the backscattering coefficient in the VH polarization is too low, close to the noise equivalent backscattering coefficient (NESZ) of the Sentinel-1 satellite. In this article, considering the influence of noise on the experimental results, all subsequent experiments are not carried out on the VH polarization but only on the VV polarization. Thereafter, saline–alkali land is used as a stable target with a low backscattering coefficient.

Since the selected saline–alkali area is uniform and has no other surface vegetation cover, taking the average of 10×10 pixel blocks is directly used to extract the backscattering coefficients to avoid errors caused by image registration during cross calibration. Because the saline–alkali land is bare, the backscattering coefficients are easily affected during the rainy season. Fig. 7 shows the time series variation of the mean backscattering coefficients under VV polarization for Dunhuang saline–alkali soil slices in 2019. The average data error for 12 scenes throughout the year is 1.53 dB. Fig. 8 shows the same data, but excludes the rainy season. After excluding the influence of the rainy season, the average error of the data for nine scenes is reduced to 0.62 dB.

C. Stable High Backscattering Target Selection and Pixel Extraction

In this article, the urban area is chosen directly as the stable target for a high backscattering coefficient. Due to the complex distribution of features in the actual urban area, the backscattering coefficients are not uniform. This article studies the influence of different extraction methods on the stability of the backscattering coefficients. It includes the stability of the median, high-frequency mean, and mean method of extracting backscattering coefficients in time series. Then we reselect the data to experiment with the extraction method. Differences between different extraction methods are shown in Fig. 9. The error is 0.82 dB when extracted by the mean method, 0.25 dB

TABLE II
STABILITY ANALYSIS OF VARIOUS GROUND OBJECT SCENES

| Scene category / Polarization	The standard deviation of backscattering coefficient (dBm^2/m^2)		The mean of backscattering coefficient (dBm^2/m^2)			
	VV	VH	VV(March)	VV(June)	VH(March)	VH(June)
Saline-alkali land	0.7700	0.5787	−16.3810	−16.3470	−23.3239	−23.3359
Desert	1.0210	0.8507	−18.1330	−17.8484	−24.7819	−24.2966
Salt lake	3.1340	3.1346	−10.9370	−14.0294	−22.1986	−25.2856
Grassland	5.8653	3.3201	−19.3547	−13.6094	−22.9662	−19.7688
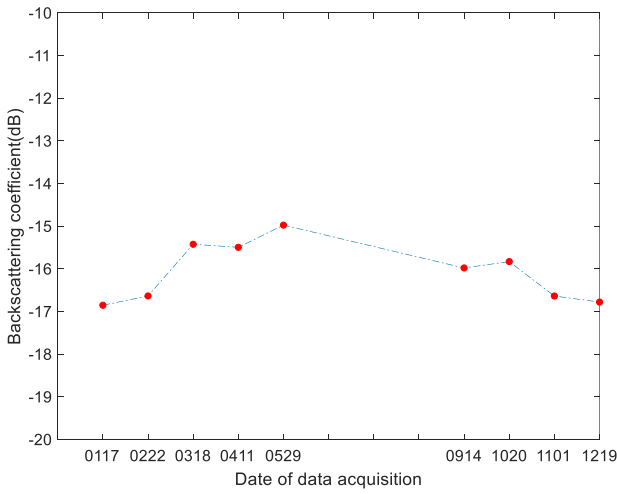
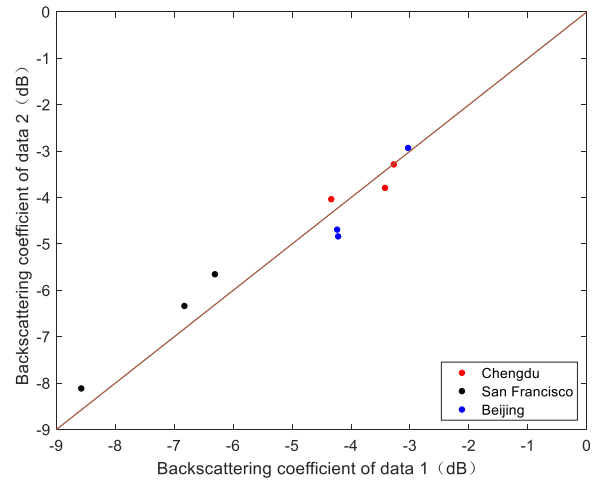Fig. 8. Time series stability analysis of saline–alkali land (excluding the influence of rainy season).

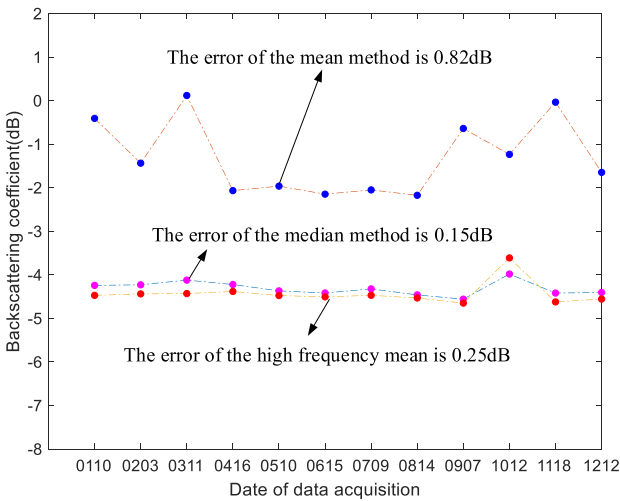Fig. 10. Influence of incidence angle on scattering characteristics in urban areas.

Fig. 9. Comparison of different extraction methods in urban areas.

Fig. 11. Correction result for incidence angle difference by the Oh model.

when extracted by the high-frequency mean method, and 0.15 dB when extracted by the median method. Therefore, the median method has been adopted.

D. Correction of Incidence Angle Difference

To verify the effect of incidence angle changes on the scattering characteristics of urban areas, this article selects two sets of data from three positions in the three cities of San Francisco, Chengdu, and Beijing. The incidence angle between every two sets of data differs by approximately 10.

The variation of scattering characteristics with incidence angle is slight in urban areas, and the error (standard deviation) is 0.4 dB, and no correction for the difference in incidence angle is applied to the urban data in the experiment. The specific experimental results are shown in Fig. 10.

TABLE III
DETAILED INFORMATION OF THE DATASET

Data	Scene category	Incidence angle	Date	Flight direction	Satellite
Data 1	Urban+ Saline-alkali land	43°(Urban), 44°(Saline-alkali land)	2017/02/14	Descending	Sentinel-1B
Data 2	Urban	43°(No correction) [1]	2017/02/20	Descending	Sentinel-1A
Data 3	Saline-alkali land	34°(With correction) [2]	2017/02/25	Descending	Sentinel-1A

[1] No correction process for incidence angle difference is performed.
[2] The correction process for incidence angle difference is performed by the method in Section III.C.
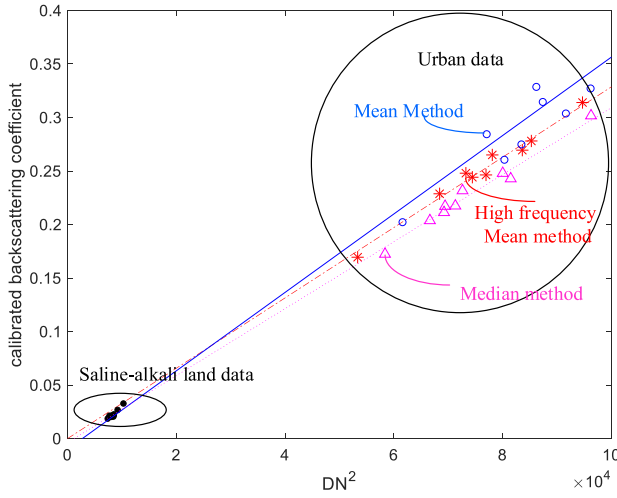

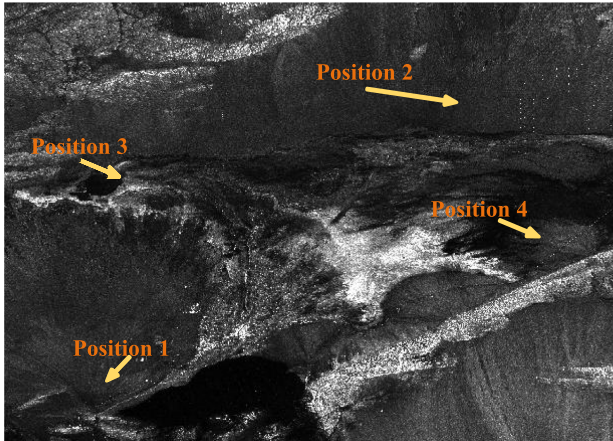Fig. 12.   Fitting calibration curve with different urban extraction methods.

Fig. 13.   Specific position of the selected target area.

The variation of scattering characteristics with incidence angle is significant in the saline–alkali area. The error (standard deviation) is 1.82 dB before correction and 0.81 dB after the Oh model-based correction using (13), as shown in Fig. 11.

E. Calculation of Calibration Coefficient

The actual data from Dunhuang is calibrated. This article calibrates Sentinel-1B data (Data 1) through Sentinel-1 A data (Data2, Data3). The backscattering coefficients of Data 1 are obtained from the backscattering coefficients of Data 2 and Data 3. The calibration dataset information is shown in Table III.

TABLE IV
CALIBRATION ACCURACY OF DIFFERENT EXTRACTION METHODS (DB)

Position / Method	Mean	Median	High-frequency mean
Position 1	1.36	0.50	1.10
Position 2	1.23	0.36	0.89
Position 3	0.77	0.30	0.68
Position 4	1.65	0.76	1.30
Average	1.25	0.48	0.99

Since the stable backscattering coefficients are extracted by the median method in the urban area, they are not sensitive to incidence angle, so the incidence angle is not corrected. In the saline–alkali area, the incidence angle of the calibrated Sentinel-1 A data and the Sentinel-1B data to be calibrated differs by about 10, and the incidence angle difference is corrected by the Oh model. After the data are prepared, the actual cross-calibration experiment is performed, and the backscattering coefficient of Sentinel-1B to be calibrated is obtained from the calibrated Sentinel-1 A data.

In the experiment, the high and low backscattering coefficients are combined to fit the calibration coefficients in the radiometric calibration formula. A total of 18 data points in urban areas and saline–alkali land were used, with 9 data points for each target.

For comparison, the median, mean, and high-frequency mean methods are used to extract urban data for radiometric calibration. The fitted calibration curves are shown in Fig. 12, where the calibration formula by the median extraction method is as follows:

$$\sigma = 3.715 \times 10^{-6} \cdot \mathrm{DN}^2 - 0.00187. \qquad (15)$$

F. Verification of Calibration Accuracy

The calibration curves (Fig. 12) fitted by different extraction methods are used to calibrate other positions' pixels in Data 1. The specific locations of the four calibration regions selected for this article are shown in Fig. 13. The data size of each region is 90×90 pixels. These four calibration regions are mainly deserts and are distributed in four different directions. They are selected following these requirements: 1) The surface must be uniform; 2) the backscattering coefficient must be greater than the noise equivalent backscattering coefficient; and 3) they must be as dispersed as possible.

In this article, the comparison between the backscattering coefficients calculated by the cross-calibration method and the backscattering coefficients actually obtained by the lookup table (LUT) [50] in the four selected regions is shown in Fig. 14.

Position 1：

Position 2：
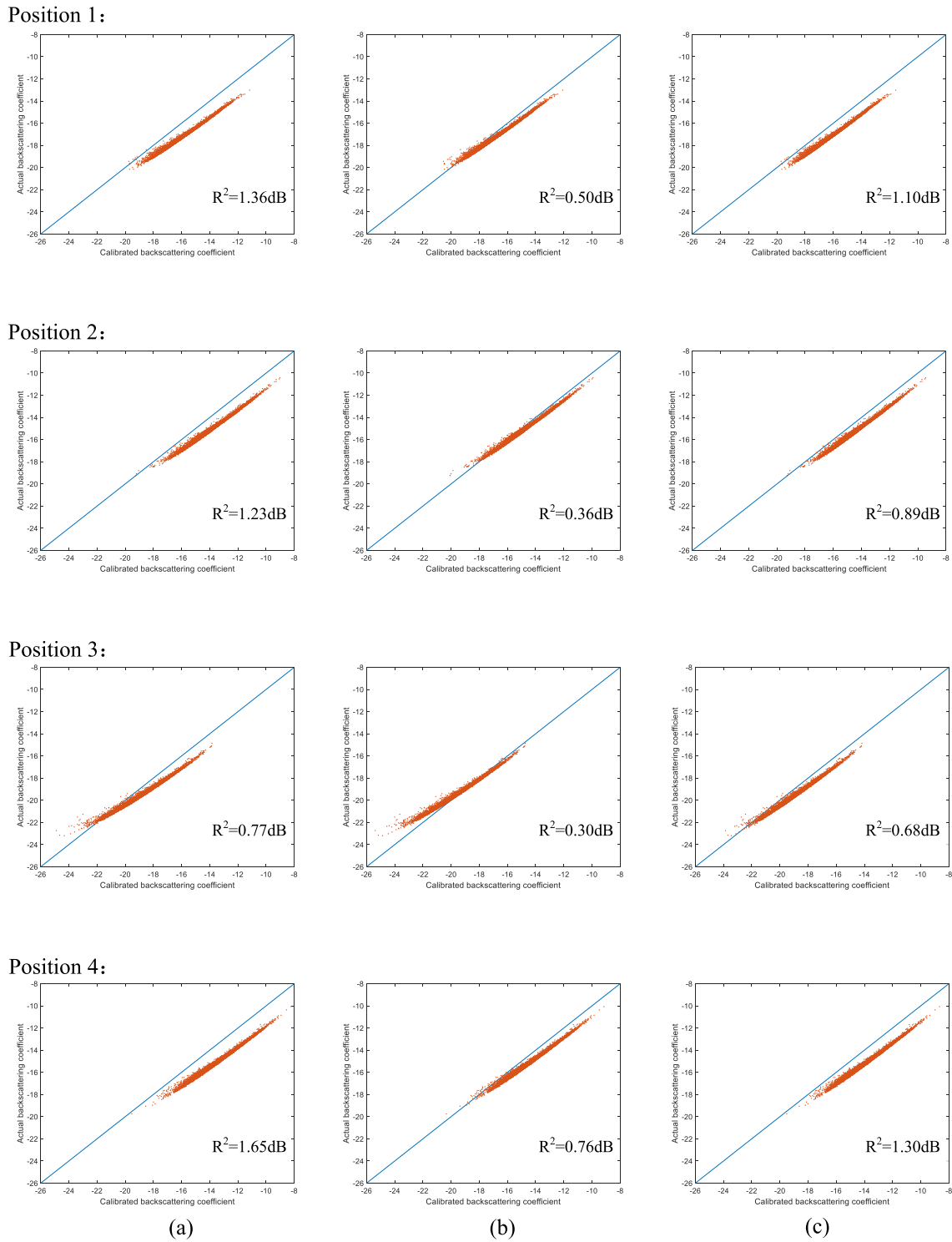
Position 3：

Position 4：

Fig. 14. Calibration accuracy of different extraction methods. (a) Mean method. (b) Median method. (c) High-frequency method.

The actual backscattering coefficient errors (standard deviation) of the four regions selected in this article are shown in Table IV.

The final accuracy of different extraction methods is obtained from the average of the actual backscattering coefficient errors of these four regions. The final calibration accuracy of the urban data extracted by the median method is 0.48 dB. The final calibration accuracy of the urban data extracted by the mean value method is 1.25 dB. The final calibration accuracy of the urban data extracted by the high-frequency mean method is 0.99 dB. The median method is the most stable for extracting urban data.

TABLE V
DETAILED INFORMATION OF THE DATASET (SAME SATELLITE)

Data	Scene category	Incidence angle	Date	Flight direction	Satellite
Data 1	Urban+ Saline-alkali land	36°(Urban), 35°(Saline-alkali land)	2018/03/18	Ascending	Sentinel-1A
Data 2	Urban	36°(No correction) [1]	2018/03/30	Ascending	Sentinel-1A
Data 3	Saline-alkali land	45°(With correction) [2]	2018/03/23	Ascending	Sentinel-1A

[1] No correction process for incidence angle difference is performed.
[2] The correction process for incidence angle difference is performed by the method in Section III.C.

TABLE VI
CALIBRATION ACCURACY OF DIFFERENT EXTRACTION METHODS (DB)

Position \ Method	Mean	Median	High-frequency mean
Position 1	0.74	0.43	0.63
Position 2	0.40	0.29	0.26
Position 3	0.90	0.30	0.38
Position 4	0.32	0.26	0.22
Average	0.59	0.32	0.37

To further verify our experimental results, we performed the same calibration experiments on Sentinel-1 A data. Dataset information is shown in Table V.

The same satellite calibration results are shown in Table VI. Fourteen scenes of saline–alkali land were used in our analytical experiments. Four saline–alkali land scenes were used for cross-calibration of the same satellite and the same series of satellites. The above experiments verify that the method in this article has good applicability in the cross-calibration of the same satellite and a series of satellites.

V. CONCLUSION

In this article, we propose a distributed target-based SAR cross radiometric calibration method to solve the problem of a limited number of artificial calibrators. The scattering in the VV polarization mode is studied. The relatively stable backscattering coefficients are obtained through the urban median extraction method and the Oh model calibration of saline–alkali land. Cross calibration is carried out through urban areas and saline–alkali land. According to the findings, the accuracy of cross calibration could reach a similar accuracy to that of the artificial calibrator-based method, and the difference was within 0.48 dB (1σ). However, the method in this article is only used for the same series of SAR satellites. For different series of satellites, their satellite parameters are quite different, which may cause significant errors in the experimental results. In future work, we will study the generality of this method and its applicability to areas other than the Dunhuang site and Sentinel-1 satellite.

ACKNOWLEDGMENT

REFERENCES

[1] A. Freeman, "SAR calibration: An overview," *IEEE Trans. Geosci. Remote Sens.*, vol. 30, no. 6, pp. 1107–1121, Nov. 1992.

[2] J. Ni, F. Zhang, Q. Yin, Y. Zhou, H.-C. Li, and W. Hong, "Random neighbor pixel-block-based deep recurrent learning for polarimetric SAR image classification," *IEEE Trans. Geosci. Remote Sens.*, vol. 59, no. 9, pp. 7557–7569, Sep. 2021.

[3] F. Ma, F. Zhang, Q. Yin, D. Xiang, and Y. Zhou, "Fast SAR image segmentation with deep task-specific superpixel sampling and soft graph convolution," *IEEE Trans. Geosci. Remote Sens.*, vol. 60, pp. 1–16, 2022.

[4] F. Ma, F. Zhang, D. Xiang, Q. Yin, and Y. Zhou, "Fast task-specific region merging for SAR image segmentation," *IEEE Trans. Geosci. Remote Sens.*, vol. 60, pp. 1–17, 2022.

[5] I. LaHaie and S. Rice, "Antenna-pattern correction for near-field-to-far field RCS transformation of 1D linear SAR measurements," *IEEE Antennas Propag. Mag.*, vol. 46, no. 4, pp. 177–183, Aug. 2004.

[6] M. Shimada, O. Isoguchi, T. Tadono, and K. Isono, "PALSAR radiometric and geometric calibration," *IEEE Trans. Geosci. Remote Sens.*, vol. 47, no. 12, pp. 3915–3932, Dec. 2009.

[7] P. Imperatore, R. Lanari, and A. Pepe, "Gical: Geo-morphometric inverse cylindrical method for radiometric calibration of SAR images," in *Proc. IEEE Int. Geosci. Remote Sens. Symp.*, 2018, pp. 7836–7839.

[8] J. van Zyl, "Calibration of polarimetric radar images using only image parameters and trihedral corner reflector responses," *IEEE Trans. Geosci. Remote Sens.*, vol. 28, no. 3, pp. 337–348, May 1990.

[9] R. Touzi, R. K. Hawkins, and S. Cote, "High-precision assessment and calibration of polarimetric RADARSAT-2 SAR using transponder measurements," *IEEE Trans. Geosci. Remote Sens.*, vol. 51, no. 1, pp. 487–503, Jul. 2013.

[10] Y. Zhou, C. Li, L. Tang, L. Ma, Q. Wang, and Q. Liu, "A permanent bar pattern distributed target for microwave image resolution analysis," *IEEE Geosci. Remote Sens. Lett.*, vol. 14, no. 2, pp. 164–168, Feb. 2017.

[11] Y. Zhou, C. Li, L. Ma, M. Y. Yang, and Q. Liu, "Improved trihedral corner reflector for high-precision SAR calibration and validation," in *Proc. IEEE Int. Geosci. Remote Sens. Symp.*, 2014, pp. 454–457.

[12] A. Babu, S. Kumar, and S. Agrawal, "Polarimetric calibration of RISAT-1 compact-pol data," *IEEE J. Sel. Topics Appl. Earth Observ. Remote Sens.*, vol. 12, no. 10, pp. 3731–3736, Oct. 2019.

[13] W. Liang, Z. Jia, J. Hong, Q. Zhang, A. Wang, and Z. Deng, "Polarimetric calibration scheme combining internal and external calibrations, and experiment for Gaofen-3," *IEEE Access*, vol. 8, pp. 7659–7671, Jan. 2020.

[14] M. Azcueta, J. P. C. Gonzalez, T. Zajc, J. Ferreyra, and M. Thibeault, "External calibration results of the SAOCOM-1 A commissioning phase," *IEEE Trans. Geosci. Remote Sens.*, vol. 60, 2021, Art. no. 5207308.

[15] S. Du, J. Hong, Y. Wang, K. Xing, T. Qiu, and J. Huang, "The influence of the azimuth RCS pattern of calibrator on SAR absolute calibration," *IEEE Geosci. Remote Sens. Lett.*, vol. 19, 2021, Art. no. 4020305.

[16] P. Slater et al., "Reflectance- and radiance-based methods for the in-flight absolute calibration of multispectral sensors," *Remote Sens. Environ.*, vol. 22, no. 1, pp. 11–37, Jun. 1987.

[17] C. Gao, X. Jiang, X. Li, and X. Li, "The cross-calibration of CBERS-02B/CCD visible-near infrared channels with Terra/MODIS channels," *Int. J. Remote Sens.*, vol. 34, no. 9/10, pp. 3688–3698, Oct. 2012.

[18] K. J. Thome, S. F. Biggar, and W. Wisniewski, "Cross comparison of EO-1 sensors and other earth resources sensors to Landsat-7 ETM+ using railroad valley playa," *IEEE Trans. Geosci. Remote Sens.*, vol. 41, no. 6, pp. 1180–1188, Jun. 2003.

[19] J. Huang, B. Yan, and N. Sun, "Monitoring of the cross-calibration biases between the S-NPP and NOAA-20 VIIRS sensor data records using GOES advanced baseline imager as a transfer," in *Proc. IEEE Int. Geosci. Remote Sens. Symp.*, 2020, pp. 6393–6396.

[20] D. Long and G. Skouson, "Calibration of spaceborne scatterometers using tropical rain forests," *IEEE Trans. Geosci. Remote Sens.*, vol. 34, no. 2, pp. 413–424, Mar. 1996.

[21] A. A. Van de Griend and E. Seyhan, "Multi-temporal analysis of ERS-1 and EMISAR c-band VV backscattering properties of forest and lake surfaces in the NOPEX region," *Agricultural Forest Meteorol.*, vol. 98-99, pp. 363–374, Dec. 1999.

[22] D. D'Aria, A. Ferretti, A. Monti Guarnieri, and S. Tebaldini, "SAR calibration aided by permanent scatterers," *IEEE Trans. Geosci. Remote Sens.*, vol. 48, no. 4, pp. 2076–2086, Apr. 2010.

[23] J. Yang, X. Qiu, C. Ding, and B. Lei, "Identification of stable backscattering features, suitable for maintaining absolute synthetic aperture radar (SAR) radiometric calibration of Sentinel-1," *Remote Sens.*, vol. 10, no. 7, Jun. 2018, Art. no. 1010.

[24] F. Zhang, X. Yao, H. Tang, Q. Yin, Y. Hu, and B. Lei, "Multiple mode SAR raw data simulation and parallel acceleration for Gaofen-3 mission," *IEEE J. Sel. Topics Appl. Earth Observ. Remote Sens.*, vol. 11, no. 6, pp. 2115–2126, Jun. 2018.

[25] F. D. Frate, A. Petrocchi, J. Lichtenegger, and G. Calabresi, "Neural networks for oil spill detection using ERS-SAR data," *IEEE Trans. Geosci. Remote Sens.*, vol. 38, no. 5, pp. 2282–2287, Sep. 2000.

[26] S. Lehner, J. Schulz-Stellenfleth, B. Schattler, H. Breit, and J. Horstmann, "Wind and wave measurements using complex ERS-2 SAR wave mode data," *IEEE Trans. Geosci. Remote Sens.*, vol. 38, no. 5, pp. 2246–2257, Sep. 2000.

[27] J. Horstmann, S. Lehner, and H. Schiller, "Global wind speed retrieval from complex SAR data using scatterometer models and neural networks," in *Proc. IEEE Int. Geosci. Remote Sens. Symp.*, vol. 3, 2001, pp. 1553–1555.

[28] G. K. Carvajal, L. E. B. Eriksson, and L. M. H. Ulander, "Retrieval and quality assessment of wind velocity vectors on the ocean with c-band SAR," *IEEE Trans. Geosci. Remote Sens.*, vol. 52, no. 5, pp. 2519–2537, May 2014.

[29] Y. Oh, K. Sarabandi, and F. Ulaby, "An empirical model and an inversion technique for radar scattering from bare soil surfaces," *IEEE Trans. Geosci. Remote Sens.*, vol. 30, no. 2, pp. 370–381, Mar. 1992.

[30] P. Dubois, J. van Zyl, and T. Engman, "Measuring soil moisture with imaging radars," *IEEE Trans. Geosci. Remote Sens.*, vol. 33, no. 4, pp. 915–926, Jul. 1995.

[31] T.-D. Wu and K.-S. Chen, "A reappraisal of the validity of the IEM model for backscattering from rough surfaces," *IEEE Trans. Geosci. Remote Sens.*, vol. 42, no. 4, pp. 743–753, Apr. 2004.

[32] N. Baghdadi, I. Gherboudj, M. Zribi, M. Sahebi, C. King, and F. Bonn, "Semi-empirical calibration of the IEM backscattering model using radar images and moisture and roughness field measurements," *Int. J. Remote Sens.*, vol. 25, no. 18, pp. 3593–3623, 2004.

[33] J. Zeng, K.-S. Chen, H. Bi, T. Zhao, and X. Yang, "A comprehensive analysis of rough soil surface scattering and emission predicted by AIEM with comparison to numerical simulations and experimental measurements," *IEEE Trans. Geosci. Remote Sens*, vol. 55, no. 3, pp. 1696–1708, Mar. 2017.

[34] S. Paloscia, S. Pettinato, and E. Santi, "Combining l and x band SAR data for estimating biomass and soil moisture of agricultural fields," *Eur. J. Remote Sens.*, vol. 45, no. 1, pp. 99–109, Feb. 2017.

[35] S. Usai and R. Klees, "SAR interferometry on a very long time scale: A study of the interferometric characteristics of man-made features," *IEEE Trans. Geosci. Remote Sens.*, vol. 37, no. 4, pp. 2118–2123, Jul. 1999.

[36] A. Ferretti, C. Prati, and F. Rocca, "Permanent scatterers in SAR interferometry," *IEEE Trans. Geosci. Remote Sens.*, vol. 39, no. 1, pp. 8–20, Jan. 2001.

[37] P. Guccione, A. M. Guarnieri, and M. Zonno, "Azimuth antenna maximum likelihood estimation by persistent point scatterers in SAR images," *IEEE Trans. Geosci. Remote Sens.*, vol. 52, no. 2, pp. 947–955, Feb. 2014.

[38] P. Guccione, M. Scagliola, and D. Giudici, "Low-frequency SAR radiometric calibration and antenna pattern estimation by using stable point targets," *IEEE Trans. Geosci. Remote Sens.*, vol. 56, no. 2, pp. 635–646, Feb. 2018.

[39] S. Du, J. Hong, Y. Wang, and Y. Qi, "Investigation of parabolic antennas as potential calibrators for spaceborne p-band POLSAR calibration," in *Proc. Asia-Pacific Conf. Synth. Aperture Radar*, 2019, pp. 1–4.

[40] P. Biancardi, L. Iannini, M. M. d'Alessandro, A. M. Guarnieri, and S. Tebaldini, "Performances and limitations of persistent scatterers-based SAR calibration," in *Proc. IEEE Radar Conf.*, 2010, pp. 762–766.

[41] B. J. Döring and M. Schwerdt, "The radiometric measurement quantity for SAR images," *IEEE Trans. Geosci. Remote Sens.*, vol. 51, no. 12, pp. 5307–5314, Dec. 2013.

[42] B. J. Döring and M. Schwerdt, "The SAR passband problem: Analytical model and possible practical solutions," *IEEE Trans. Geosci. Remote Sens.*, vol. 54, no. 3, pp. 1647–1658, Mar. 2016.

[43] R. Moore, V. Westmoreland, D. Frank, and M. Hemmat, "Determining the vertical antenna pattern of a spaceborne SAR by observation of uniform targets," in *Proc. IEEE Int. Geosci. Remote Sens. Symp.*, vol. 1, 1986, pp. 469–472.

[44] J.-J. Zhang, W. Hong, and Y.-Q. Jin, "On the method of polarimetric SAR calibration using distributed targets," *IEEE Trans. Geosci. Remote Sens.*, vol. 60, 2022, Art. no. 5202316.

[45] A. Zakharov and L. Zakharova, "PALSAR calibration with distributed targets," in *Proc. IEEE Int. Geosci. Remote Sens. Symp.*, 2019, pp. 8328–8331.

[46] M. Zink, P. Olivier, and A. Freeman, "Cross-calibration between airborne SAR sensors," *IEEE Trans. Geosci. Remote Sens.*, vol. 31, no. 1, pp. 237–245, Jan. 1993.

[47] A. Zakharov, P. Zherdev, and A. Sokolov, "Intercalibration of ERS AMI and ENVISAT ASAR with ground-based parabolic antennas," in *Proc. Envisat ERS Symp. Citeseer*, 2004, pp. 6–10.

[48] S. Shangguan, X. Qiu, J. Yang, B. Lei, and C. Din, "Extraction and analysis of the scattering stability in urban areas based on dual-polarization SAR data," *IEEE Geosci. Remote Sens. Lett.*, vol. 16, no. 3, pp. 427–431, Mar. 2019.

[49] N. Miranda et al., "Sentinel-1 A/B SAR calibration and performance status," in *Proc. Eur. Conf. Synth. Aperture Radar*, 2021, pp. 1–4.

[50] "S-1 A & S-1B annual performance report for 2021," Collecte Localisation Satellites, Toulouse, France, MPC-0504, 2021, [Online]. Available: https://sentinel.esa.int/documents/247904/4776206/DI-MPC-APR-523-1-1-Annual%20Performance%20Report%202021.pdf/9a5bf9a7-b8b7-4b6b-e3c0-ce23bdb565b8

Yongsheng Zhou (Member, IEEE) received the B.E. degree in communication engineering from Beijing Information Science and Technology University, Beijing, China, in 2005, and the Ph.D. degree in signal and information processing from the Institute of Electronics, Chinese Academy of Sciences, Beijing, China, in 2010.

He was with Academy of Opto-Electronics, Chinese Academy of Sciences, during 2010 and 2019, and is currently a Professor of Electronic and Information Engineering with the College of Information Science and Technology, Beijing University of Chemical Technology, Beijing, China. His research interests include target detection and recognition from microwave remotely sensed image, digital signal, and image processing.

Li Zhuang received the M.S. degree in information and communication engineering from the College of Information Science and Technology, Beijing University of Chemical Technology, Beijing, China, in 2022.

Her research interests include SAR image processing and SAR radiometric cross calibration.

Jitong Duan received the B.E. degree in telecommunication engineering from the Beijing University of Posts and Telecommunications, Beijing, China, in 2017, and the M.S. degree in mechanical engineering from the University of Minnesota Twin Cities, Minneapolis, MN, USA, in 2020.

She is currently a Research Assistant with the Key Laboratory of Technology in Geo-spatial Information Processing and Application System, Aerospace Information Research Institute, Chinese Academy of Sciences, Beijing, China. Her research interests include synthetic aperture radar image processing and radiometric calibration.

Fan Zhang (Senior Member, IEEE) received the B.E. degree in communication engineering from the Civil Aviation University of China, Tianjin, China, in 2002, the M.S. degree in signal and information processing from Beihang University, Beijing, China, in 2005, and the Ph.D. degree in signal and information processing from the Institute of Electronics, Chinese Academy of Sciences, Beijing, in 2008.

He is a Full Professor of electronic and information engineering with the Beijing University of Chemical Technology, Beijing, China. His research interests include remote sensing image processing, high-performance computing, and artificial intelligence.

Dr. Zhang is also an Associate Editor for IEEE ACCESS and a Reviewer for the IEEE TRANSACTIONS ON GEOSCIENCE AND REMOTE SENSING, the IEEE JOURNAL OF SELECTED TOPICS IN APPLIED EARTH OBSERVATIONS AND REMOTE SENSING, the IEEE GEOSCIENCE AND REMOTE SENSING LETTERS, and the *Journal of Radars*.

Wen Hong (Senior Member, IEEE) received the M.S. degree in electronic engineering from Northwestern Polytechnical University, Xi'an, China, in 1993, and the Ph.D. degree from Beihang University, Beijing, China, in 1997.

From 1997 to 2002, she was a Faculty Member in signal and information processing with the Department of Electrical Engineering, Beihang University. In between, she was a Guest Scientist with DLR-HF, Wessling, Germany, from 1998 to 1999, for one year. Since 2002, she has been a Scientist with the Aerospace Information Research Institute, Chinese Academy of Sciences, Beijing, China. Her research interests include polarimetric/polarimetric interferometric synthetic aperture radar (SAR) data processing and application, 3-D SAR signal processing, circular SAR signal processing, SAR polarimetric application, and sparse microwave imaging with compressed sensing.